

# Instability of electrokinetic microchannel flows with conductivity gradients

Hao Lin<sup>a)</sup>

*Department of Mechanical Engineering, Stanford University, Stanford, California 94305*

Brian D. Storey

*Franklin W. Olin College of Engineering, Needham, Massachusetts 02492*

Michael H. Oddy, Chuan-Hua Chen, and Juan G. Santiago

*Department of Mechanical Engineering, Stanford University, Stanford, California 94305*

(Received 11 August 2003; accepted 18 February 2004; published online 29 April 2004)

Electrokinetic flow is leveraged in a variety of applications, and is a key enabler of on-chip electrophoresis systems. An important sub-class of electrokinetic devices aim to pump and control electrolyte working liquids with spatial gradients in conductivity. These high-gradient flows can become unstable under the application of a sufficiently strong electric field. In this work the instability physics is explored using theoretical and numerical analyses, as well as experimental observations. The flow in a long, rectangular-cross-section channel is considered. A conductivity gradient is assumed to be orthogonal to the main flow direction, and an electric field is applied in the streamwise direction. It is found that such a system exhibits a critical electric field above which the flow is highly unstable, resulting in fluctuating velocities and rapid stirring. Modeling results compare well with experimental observations. The model indicates that the fluid forces associated with the thin dimension of the channel (transverse to both the conductivity gradient and the main flow direction) tends to stabilize the flow. These results have application to the design and control of on-chip assays that require high conductivity gradients, and provides a rapid mixing mechanism for low Reynolds number flows in microchannels. © 2004 American Institute of Physics.

[DOI: 10.1063/1.1710898]

## I. INTRODUCTION

Over the past decade there has been extensive research into the design of microfluidic systems for chemical analysis. These devices offer the promise of integrating multiple laboratory processes onto a single chip, thereby increasing throughput and decreasing assay cost.<sup>1</sup> Extensive reviews of manufacturing techniques, applications, and engineering challenges of micro total analysis systems ( $\mu$ TAS) have been presented.<sup>2–5</sup>

The mass and ion transport regimes of  $\mu$ TAS are often distinct from macro-scale flow devices. One important regime is electrokinetics (EK), which describes the coupling of ion transport, fluid flow, and electric fields.<sup>6,7</sup> A solid surface in contact with an electrolyte typically acquires a surface charge and forms an electric double layer (EDL), composed of the wall charge and a counter-ion shielding layer with a thickness characterized by the Debye length. Electroosmosis is the bulk motion of liquid that results upon the application of an external field with a component parallel to the surface. Electrokinetics includes also electrophoresis, which is the drift motion of charged species.

Typical microchannel flows have characteristic scales of 10 microns or greater, and Debye lengths of 10 nm or less, so that the EDL is confined to a thin layer near the wall. For “thin” EDLs, electrolyte motion outside of the double layer can be modeled as flow with a slip velocity condition.<sup>8</sup> This

slip approximation is unlike the stress-free condition of potential flow theory<sup>9</sup> in that it supports both a slip velocity proportional to local electric field and a viscous stress. As we shall discuss here, net charge can also be generated in the bulk flow due to the interaction of electric fields and conductivity gradients; this leads to body forces that can destabilize electrokinetic flow.<sup>10,11</sup>

Electrokinetics is a subfield of electrohydrodynamics (EHD), which can be defined as the interaction between electric fields and fluid motion. Generalized transport equations for EHD flows are presented in a review by Saville.<sup>12</sup> EK effects are distinguished by the importance of charge separation at solid–liquid interfaces.<sup>7,13,14</sup> These interfacial forces can dominate solute transport in  $\mu$ TAS. General EHD theory also includes forces that act away from solid–liquid interfaces in regions where the liquid has conductivity and permittivity gradients.<sup>15</sup> Classical EHD studies typically deal with near-dielectric liquids with conductivities of order  $10^{-11}$ – $10^{-9}$  S/m and can be described by the leaky-dielectric model developed by Taylor and Melcher.<sup>12</sup> In this model, liquids are described as having both polarizability and free charge, and the internal electric field generated by accumulated charges can be on the order of the externally imposed field. The leaky-dielectric model is reviewed in detail by Saville<sup>12</sup> and Melcher and Taylor.<sup>15,16</sup> The model often uses a formulation for conservation of net charge and conductivity as scalar quantities.<sup>15</sup> This Ohmic model has been used to describe instabilities in EHD flows where interfacial EK effects are not considered.<sup>17</sup> This work includes

<sup>a)</sup>Electronic mail: hao.lin@stanford.edu

EHD stability studies with axial (i.e., parallel to an electric field),<sup>11,18</sup> and transverse conductivity gradients.<sup>10</sup>

We shall apply concepts from generalized EHD theory to describe EK flow instabilities in microchannels. Particularly relevant to our work is that of Hoburg and Melcher,<sup>10</sup> who studied a similar flow configuration and electric field configuration. They performed a stability analysis for an electric field parallel to a liquid–liquid interface (perpendicular to the conductivity gradient) and flow initially at rest. Their analysis, which neglects molecular diffusion, showed the interface is stable for all electric fields when the liquid–liquid interface is assumed to be infinitely sharp.<sup>19</sup> More importantly, they showed this configuration is unstable for all applied electric fields when the interface is modeled with a finite-width, exponentially dependent concentration profile between the two liquids (with no subsequent diffusion). The latter case exhibited an instability that resulted in buckling and distortion of the interface. Hoburg and Melcher described the instability mechanism as initiated by charge accumulation at a perturbed interface, and made qualitative comparisons to experiments with an oil–oil interface contained between two 19 by 70 mm glass plates separated by 4 mm in the direction perpendicular to both the applied field and the conductivity gradient, and a characteristic field of  $\sim 10^4$  V/cm.<sup>10</sup> Another important insight is offered by the work of Baygents and Baldessari<sup>11</sup> who found that including the diffusion of conductivity is crucial to the existence of a critical electrical field above which the flow is unstable. Although their conclusion was reached for a different electric field/conductivity gradient configuration, we will show the idea also holds for our case. (A study of a flow field similar to that considered by Baygents and Baldessari was also performed by Ben *et al.*,<sup>20</sup> using a similarity analysis approach; however, these authors concluded that flow instabilities were insignificant for their parameter range of interest.)

Here we are interested in EK flows with conductivity gradients, which are critical to a variety of on-chip assays including field amplified sample stacking,<sup>21</sup> isoelectric focusing,<sup>22</sup> and electrophoretic assays where conductivities of various sample and buffer streams are either unknown or poorly controlled. This flow also has direct applications to rapid mixing of sample streams and to preserving the stability of co-flowing streams as in lamination processes.<sup>23</sup> A fundamental understanding of electrokinetic instabilities can provide a design framework whereby instabilities are avoided, as they are often detrimental to system performance. Two of us (C.H.C. and J.G.S.) reported observations of EK instabilities in flows with significant conductivity gradients within microfluidic T- and X-junctions.<sup>24</sup> Three of us (C.H.C., H.L., J.G.S. together with S. K. Lele) presented a formulation of these instability dynamics and summarized the results of a linear analysis that models the mechanism behind the growth and propagation of the unstable waves in EK T-junctions.<sup>25</sup> These instabilities can also be applied as a means for rapid mixing of low Reynolds number flows, where mixing is often limited by molecular diffusion.<sup>26</sup> For example, two of us (M.H.O. and J.G.S.) have leveraged electrokinetic instabilities in a rapid micromixer design.<sup>27</sup>

In this paper we present experimental, analytical, and computational results in order to quantify an electrokinetic flow instability observed in long, thin electrokinetic microchannels with conductivity gradients orthogonal to the channel axis. We will re-exam the assumptions of Hoburg and Melcher for micro-fluidic applications, and follow a general formulation and framework given by Melcher.<sup>15</sup> In particular, we include advective effects due to electroosmotic flow, an initial conductivity profile consistent with our experiments, and a diffusive component of the conductivity conservation equation critical in modeling EK instabilities. The electroosmotic flow results in a shear flow imposed on the liquid. The detailed physics of the EDL are treated as coupled to the rest of the flow through a slip boundary condition which depends on local electrolyte conductivity. We present a two-dimensional linear stability analysis and conduct nonlinear flow simulations. We also extend the linear analysis to include three-dimensional effects.

The paper is organized as follows. In Sec. II we outline our flow field and present experimental results; in Sec. III we formulate the governing equations; in Sec. IV we present a two-dimensional model, conduct a linear stability analysis, present stability diagrams in the phase space of wave number and the applied electrical field, and present full numerical simulations; in Sec. V we perform analysis of the three-dimensional flow and perform linearized numerical simulations to find stability boundaries. We discuss the differences between the flow dynamics in the two- and three-dimensional cases, demonstrate the mechanisms for the instability and compare theory to experiments in Sec. VI.

## II. EXPERIMENTAL OBSERVATIONS

### A. Setup

Figure 1 shows a schematic of the microchannel setup used in the experiments. The microchannel consisted of a borosilicate glass capillary (Wilmad-Labglass, NJ) with a rectangular cross section; the inner dimensions were 1 mm  $\times$  100  $\mu$ m, and the length was 40 mm. The capillary ends were sealed using a silicone adhesive to custom-machined acrylic manifolds housing inlet and outlet ports. A syringe pump forced dyed and undyed buffer solutions from the inlet ports through the capillary toward the outlet port. The buffered solutions completed the electric circuit between platinum electrodes located at the inlet and outlet of the capillary. The aqueous buffered solutions consisted of a 10 mM HEPES buffer (Sigma-Aldrich Corp, MO). To visualize fluid motion, an electrically neutral, high-molecular-weight dye (70kDalton) composed of a dextran-rhodamine B conjugate (Molecular Probes, OR) was added to one of the buffer streams at a concentration of 2  $\mu$ M. This dye was used to minimize both electrophoretic drift and molecular diffusion of dye molecules during experiments of order 10 s duration. The dynamics of the scalar fields shown here are, therefore, associated with the development of the background bulk liquid. Potassium chloride was added to the dyed buffer solution to control/increase its electrical conductivity. The dyed solution conductivity,  $\sigma_{\text{high}}$ , was measured as 50  $\mu$ S/cm using a CON 500 Oakton Instruments conductivity meter (Ver-

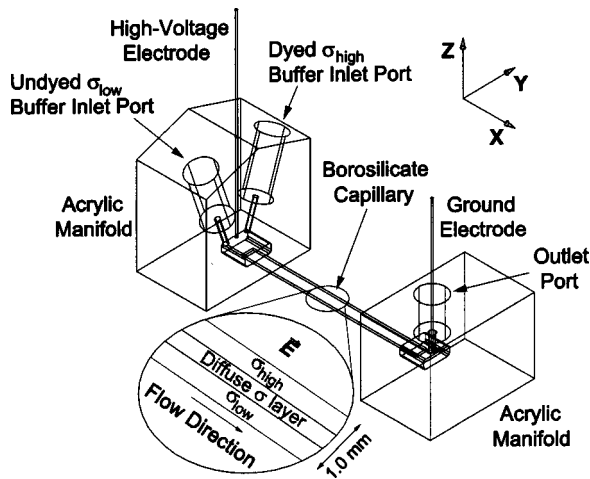


FIG. 1. Schematic of the setup used for microchannel flow experiments. The channel is 1 mm wide ( $y$ ), 100  $\mu\text{m}$  deep ( $z$ ), and 40 mm long ( $x$ ). Two buffer solutions with differing electrical conductivities are introduced into the microchannel using a syringe pump, resulting in a single buffer stream with a spanwise electrical conductivity gradient. Upon the application of a high voltage along the streamwise direction, the width of the diffuse conductivity interface is approximately 750  $\mu\text{m}$  at the imaging location, halfway between the inlet and outlet of the capillary. The shape and thickness of the conductivity field is derived from the residence time of the interface in the channel ( $\sim 12$  s) before the activation of the electric field and as it flows from the inlet to the viewing area.

non, IL), while that of the undyed buffer solution,  $\sigma_{\text{low}}$ , was 5  $\mu\text{S}/\text{cm}$ , yielding a conductivity ratio of  $\gamma=10$ . The dilute electrolytes can be assumed to have the permittivity and viscosity of pure water.<sup>28,29</sup> Other properties of the working electrolytes are discussed in Sec. III, and summarized in Table I.

The two syringes on the syringe pump were loaded with high and low conductivity liquid. These two outputs were connected to the upstream manifold which combined the pressure-driven streams of the syringes into the glass microchannel, forming an interface within the channel. The two buffer streams initially occupied the upper and lower halves of the microchannel resulting in a diffuse conductivity gradient along the spanwise,  $y$ -direction. Following buffer

stream injection, the syringe pump was deactivated and the electric potential of the inlet port electrode was raised while keeping the outlet port electrode grounded. The imposed electric potential initiated an electroosmotic flow in the channel and, for electric fields above a threshold value, electrokinetic instabilities. The potential drop between the electrodes was held constant at 1, 2, or 3 kV using a voltage signal from a LabVIEW-controlled DAQ card (National Instruments Inc.) coupled to a high voltage amplifier (10/10b, Trek Inc., NJ). Fluid motions were observed using an inverted, epi-fluorescent microscope (Nikon TE300) and a 4 $\times$  microscope objective (numerical aperture of 0.2). To increase the field of view, a 0.6 $\times$  demagnifying lens was used, resulting in an overall magnification of 2.4 $\times$ . A CCD camera (CoolSnap fx, Roper Scientific Inc., AZ) with a 12-bit intensity digitization resolution recorded the images. Image signal-to-noise ratio and frame rate was improved by binning individual CCD pixels to form 4 $\times$ 4 super pixels, which resulted in final binning dimensions of 26.8 $\times$ 26.8  $\mu\text{m}$  in the image plane. The exposure time and frame rate were, respectively, 15 ms and 10 frames per second.

## B. Results

A representative set of images from experiments conducted at 1, 2, and 3 kV applied potentials are shown in Fig. 2. The potentials were applied over the 40 mm channel length; these were equivalent to applied fields of 25000, 50000, and 75000 V/m, respectively. In each case, the top figure of each series shows the initial, undisturbed interface between the dyed and undyed buffer streams in the channel ( $t=0$ ). The successive images in each column show the temporal evolution of the imaged dye under a constant, DC potential. In this color scheme, blue corresponds to the undyed, low-conductivity stream, and red to the dyed high conductivity stream. For a field of 25000 V/m, the interface was only slightly perturbed and only slight fluctuations were apparent in the images captured at 4.0 and 5.0 s. At the two higher applied potentials, the interface exhibited a rapidly growing wave pattern within the first 0.5 s. The unstable fluid motion in the channel buckled the interface and proceeded to stretch and fold material lines. The transverse and fluctuating velocities associated with this unstable motion resulted in rapid mixing of the two streams. At the 75000 V/m applied field, the channel reached a well-stirred state with nearly homogeneous concentration fields observable within 5 s. Qualitatively, the observed dynamics of the interface may be described as follows: First, the interface buckled into a wave-like pattern with spatial wavelengths ranging from 1 to 2 times of the spanwise channel width. Next, low-intensity, unseeded regions extended into the dyed region of the flow in a series of finger-like structures aligned with the concentration minima in the initial wave (e.g., see the 1.0 s image at 50000 V/m and, especially, the 0.5 s image at 75000 V/m). Next, the interface and fingering structures broke down into a more complex pattern with concentration fluctuations occupying the full width of the channel. At this late stage, rolling structures were sometimes apparent. Finally, as the complex velocities associated with the instability

TABLE I. Parameters and fundamental scales.

Symbol	Description	Value
$\epsilon_0$	Universal permittivity coefficient	$8.85 \times 10^{-12}$ C/V $\cdot$ m
$\epsilon_r$	Relative permittivity	78.3
$\epsilon$	Permittivity	$6.93 \times 10^{-10}$ C/V $\cdot$ m
$\mu$	Absolute viscosity	$10^{-3}$ kg/m $\cdot$ s
$\rho_0$	Density for water	$10^3$ kg/m $^3$
$D$	Diffusivity	$2.0 \times 10^{-9}$ m $^2$ /s
$w$	Mobility	$8.2 \times 10^{-13}$ mol $\cdot$ s/kg
$F$	Faraday constant	$9.65 \times 10^4$ C/mol
$\zeta_0$	Reference EDL zeta potential	$-7.0 \times 10^{-2}$ V
$\Delta C_0$	Molar concentration difference	$3.7 \times 10^{-7}$ mol/m $^3$
$C_0$	Molar concentration	$3.3 \times 10^{-2}$ mol/m $^3$
$H$	Half-width of the channel	$5.0 \times 10^{-4}$ m
$E_0$	Typical value for impose field	$2.5 \times 10^4$ V/m
$U_{ev}$	Electroviscous velocity scale	$2.2 \times 10^{-1}$ m/s
$T$	Time scale	$2.4 \times 10^{-2}$ s

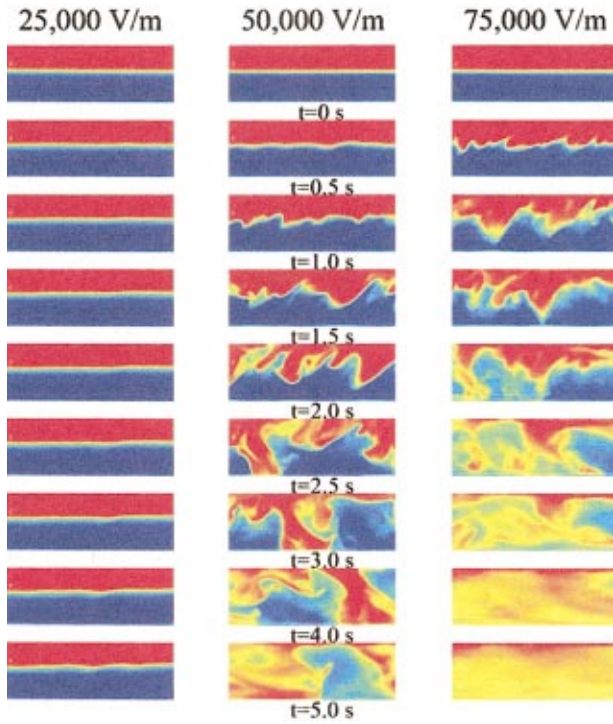


FIG. 2. (Color) Sample images from the experiment, shown for applied fields of 25000, 50000, and 75000 V/m, corresponding to the first, second, and third column. Images obtained at various times are shown for each column. The electric field and bulk flow directions were from left to right. High voltage was applied as a Heaviside function at  $t=0$  s. Each image corresponds to a physical area 1 mm wide ( $y$ ) and 3.6 mm long ( $x$ ). The depth of the channel is 100  $\mu\text{m}$  along the  $z$  direction (into the page). At the time of the application of the high voltage, the diffuse conductivity interface was approximately 750  $\mu\text{m}$  wide at the imaging location. Small amplitude waves observed at  $t=0.5$  s quickly grow and lead to rapid stirring of the initially distinct buffer streams. The instability quickly stretches and folds material lines and, after about 4 s for the 75000 V/m applied field, results in a well-stirred, relatively homogeneous dye concentration field. The time of the images in each row are shown in the figure.

stretched and folded material lines, the dye distributed evenly throughout the channel, making it difficult to further observe liquid motion. The largest transverse velocities in the experiments (observable by the initial transverse motion of the interface) were roughly 0.1–5 mm/s for applied fields of 25000–75000 V/m. Again note that diffusive transport of the dye in this experiment was negligible so that the homogeneous dye concentration at the later times of the 50000 and 75000 V/m experiments were indicative of a well-stirred state.

### III. THEORETICAL FORMULATION

The description of experiments given above serves as an introduction to the problem and describes observed features of electrokinetic flow instability. We now turn to a theoretical formulation of the flow following a general framework provided by Melcher.<sup>15</sup> We start with general charge conservation equations, perform scaling analysis, and obtain a set of simplified equations that is suitable for the parameter range of our experiments.

### A. Governing equations

We start with the conservation laws for a dilute, two-species electrolyte solution:<sup>15</sup>

$$\frac{\partial C_1}{\partial t} + \mathbf{v} \cdot \nabla C_1 = w_1 \nabla \cdot (z_1 F C_1 \nabla \Phi) + D_1 \nabla^2 C_1, \quad (1)$$

$$\frac{\partial C_2}{\partial t} + \mathbf{v} \cdot \nabla C_2 = w_2 \nabla \cdot (z_2 F C_2 \nabla \Phi) + D_2 \nabla^2 C_2, \quad (2)$$

where  $C_i$ 's are the molar concentration of the electrolytes,  $w_i$ 's are the coefficients of mobility,  $F$  is the Faraday constant,  $D_i$ 's are the diffusive coefficients,  $z_i$ 's are the valence numbers (we assume  $z_1 = -z_2 = 1$ ), and  $\Phi$  is the electric potential. The Poisson equation for the electric field is then

$$\epsilon \nabla^2 \Phi = -\rho_E, \quad (3)$$

where

$$\rho_E = \sum_{i=1}^2 z_i F C_i. \quad (4)$$

Here  $\rho_E$  is the charge density, and  $\epsilon = \epsilon_r \epsilon_o$  is the permittivity of the liquid. In the Poisson formulation, we assume the permittivity of the liquid is uniform as we are interested in nearly isothermal electrokinetic microflows of dilute electrolytes (e.g., biological buffers with order 10 mM concentrations). In such systems, electrolyte conductivity field is dominated by ion densities and a uniform ion mobility, and electrolyte permittivity is that of the solvent (typically water). To complete the system we need also the continuity and conservation of momentum equations for the liquid,

$$\nabla \cdot \mathbf{v} = 0, \quad (5)$$

$$\rho \left( \frac{\partial \mathbf{v}}{\partial t} + \mathbf{v} \cdot \nabla \mathbf{v} \right) = -\nabla p + \mu \nabla^2 \mathbf{v} - \rho_E \nabla \Phi. \quad (6)$$

Here,  $\rho$  is the density,  $\mathbf{v}$  is the flow velocity,  $p$  is the pressure, and  $\mu$  is the absolute viscosity. The electric flux and species conservation are coupled to the mechanics through the electric force  $-\rho_E \nabla \Phi$  in the momentum equation.

For our problem it is more convenient to transform the system of molar concentrations ( $C_1, C_2$ ) into the quantities of  $(\rho_E, \sigma)$ , using Eq. (4) and the definition for conductivity

$$\sigma \equiv \sum_i w_i z_i^2 F^2 C_i. \quad (7)$$

For the simple case of two species, Eqs. (4) and (7) constitute a reversible transformation from the pair  $(C_1, C_2)$  into  $(\rho_E, \sigma)$ , with the inverse transform

$$C_1 = \frac{\sigma + w_2 F \rho_E}{F^2 (w_1 + w_2)},$$

$$C_2 = \frac{\sigma - w_1 F \rho_E}{F^2 (w_1 + w_2)}.$$

If we further assume, for simplicity, that other properties of the electrolytes are symmetric, i.e.,  $w_1 = w_2 = w$ ,  $D_1 = D_2 = D$ , and  $z_1 = -z_2 = 1$ , we can re-write Eqs. (1) and (2) in terms of  $\rho_E$  and  $\sigma$ , as

$$\frac{\partial \rho_E}{\partial t} + \mathbf{v} \cdot \nabla \rho_E = \nabla \cdot (\sigma \nabla \Phi) + D \nabla^2 \rho_E, \quad (8)$$

$$\frac{\partial \sigma}{\partial t} + \mathbf{v} \cdot \nabla \sigma = F^2 w^2 \nabla \cdot (\rho_E \nabla \Phi) + D \nabla^2 \sigma. \quad (9)$$

Equations (8) and (9), together with (3), (5), (6), and appropriate boundary conditions, completely define our system of interest.

## B. Scaling and simplifications

We introduce the following scales for the nondimensionalization of our governing equations:

$$\begin{aligned} [\mathbf{v}] &= U_{ev}, \quad [L] = H, \quad [t] = H/U_{ev}, \\ [\sigma] &= w F^2 C_o, \quad [\Phi] = E_o H, \quad [\rho_E] = F \Delta C_o, \\ [\rho] &= \rho_o, \quad [p] = \mu U/H, \quad [\zeta] = \zeta_o. \end{aligned}$$

Here  $\zeta$  is the EDL zeta potential (discussed below). The values we adopt for these scales are listed in Table I, and are chosen to best represent the experiments in Sec. II. The ion diffusivity and mobilities are averages of the values of potassium chloride ions which dominate the conductivity field.

A few remarks on the value of the scales we choose are appropriate. First, the scale for the charge density is chosen such that the electric field generated by charges in the bulk matches the imposed one in magnitude [see Eq. (3)]:

$$F \Delta C_o = \frac{\epsilon E_o}{H},$$

or

$$\frac{\Delta C_o}{C_o} = \frac{\epsilon E_o}{F C_o H} \sim 1.0 \times 10^{-5}.$$

The choice of characteristic length in this relation is appropriate as we are interested in cases where the diffusive length scale is on the order of the spanwise channel width  $H$ . Because the charge density is induced by the molar difference of the two species, the smallness of the parameter  $\Delta C_o/C_o$  implies the well-known electroneutrality assumption.<sup>10,11,15</sup> This assumption states an approximately net neutral condition of the form

$$C_1 \approx C_2.$$

However, the finite difference between the concentration of the two species is proportional to the net charge in the system and, although small compared to  $C_o$ , can easily generate a significant electric body force term that must be considered in the equations of fluid motions. (We have confirmed with nonlinear numerical simulations of these equations that the generated field in unstable–rapid mixing conditions is comparable to or greater than the applied field in magnitude.) Second, the velocity scale is derived from the balance of viscous force with the electric body force in the momentum equation (6), following Hoburg and Melcher:<sup>10</sup>

$$U_{ev} \equiv \frac{\epsilon E_o^2 H}{\mu}. \quad (10)$$

Note that we do not use the apparent, “obvious” velocity scale that is observed experimentally in the base flow, that is, the electroosmotic velocity

$$U_{eo} \equiv -\frac{\epsilon \zeta_o E_o}{\mu}. \quad (11)$$

This is the well-known Helmholtz–Smoluchowski formulation which we use to relate electroosmotic velocity to the wall zeta potential and electric field. This velocity is established within the EDL and determines the bulk advection of scalars in the flow field. However, as we will show later in Sec. IV, for the unstable, rapid-mixing regime of interest here, the electroviscous velocity scale  $U_{ev}$  is correct in characterizing the fluctuations associated with EK instabilities.

Our governing equations in dimensionless form then read

$$\frac{\Delta C_o}{C_o} \left( \frac{\partial \rho_E}{\partial t} + \mathbf{v} \cdot \nabla \rho_E \right) = \beta \nabla \cdot (\sigma \nabla \Phi) + \frac{\Delta C_o}{Ra_e C_o} \nabla^2 \rho_E, \quad (12)$$

$$\frac{\partial \sigma}{\partial t} + \mathbf{v} \cdot \nabla \sigma = \frac{\Delta C_o}{C_o} \beta \nabla \cdot (\rho_E \nabla \Phi) + \frac{1}{Ra_e} \nabla^2 \sigma, \quad (13)$$

$$\nabla^2 \Phi = -\rho_E, \quad (14)$$

$$\nabla \cdot \mathbf{v} = 0, \quad (15)$$

$$Re \left( \frac{\partial \mathbf{v}}{\partial t} + \mathbf{v} \cdot \nabla \mathbf{v} \right) = -\nabla p + \nabla^2 \mathbf{v} - \rho_E \nabla \Phi, \quad (16)$$

where

$$Ra_e \equiv \frac{U_{ev} H}{D} = \frac{\epsilon E_o^2 H^2}{\mu D} \sim 5.4 \times 10^4, \quad (17)$$

is an electric Rayleigh number (this use of Rayleigh number to denote the ratio of diffusive to convective time scale is similar to that by Baygents and Baldessari),<sup>11</sup>

$$Re \equiv \frac{\rho_o U_{ev} H}{\mu} = \frac{\rho_o \epsilon E_o^2 H^2}{\mu^2} \sim 100, \quad (18)$$

is the Reynolds number. The dimensionless number  $\beta$  is defined as

$$\beta \equiv \frac{w F E_o}{U_{ev}} \sim 9 \times 10^{-3}, \quad (19)$$

which is the ratio of the electrophoretic ion velocity to the electroviscous flow velocity.

We should mention that as the magnitude of the imposed field (and subsequently the scale  $E_o$ ) changes, the dimensionless numbers  $\Delta C_o/C_o$ ,  $\beta$ ,  $Ra_e$ , and  $Re$  change as well, and the flow can be brought into different regimes. However, for the electric field range of interest,  $\Delta C_o/C_o$  remains a very small quantity, which results in further simplifications of our system.<sup>36</sup> Namely, the divergence term is dominant in Eq. (12), so the equation reduces to

$$\nabla \cdot (\sigma \nabla \Phi) = 0. \quad (20)$$

This relaxation assumption states that the generated field instantaneously satisfies the divergence condition. If we decompose the electric field into a constant, imposed, unidirectional field plus a generated one as  $\mathbf{E} = E_o \mathbf{e}_x - \nabla \phi$  in dimensional form (or  $\mathbf{E} = \mathbf{e}_x - \nabla \phi$  in nondimensional form), we obtain

$$\frac{\partial \sigma}{\partial x} = \nabla \cdot (\sigma \nabla \phi). \quad (21)$$

We denote the generated field with  $\phi$ , and distinguish it from the total (applied *plus* generated) field  $\Phi$ . Consequently, Eq. (13) can be simplified as

$$\frac{\partial \sigma}{\partial t} + \mathbf{v} \cdot \nabla \sigma = \frac{1}{Ra_e} \nabla^2 \sigma, \tag{22}$$

which is a natural consequence out of the electroneutrality condition.

Equations (14)–(16), (21), and (22) constitute a complete system for  $\sigma$ ,  $\rho_E$ ,  $\phi$ ,  $p$ , and  $\mathbf{v}$ , and will be the set of governing equations.

It is instructive to compare this formulation for EK flow instabilities to previous work on EHD flow instabilities. First, the inclusion of the diffusive term in the conservation of conductivity equation (22) is suggested by the work of Baygents and Baldessari.<sup>11</sup> Although they examined a different electric field and conductivity gradient configuration, Baygents and Baldessari found that molecular diffusion had an important stabilizing effect and is responsible for the existence of a threshold electric field below which their EHD flow was stable. Our modeling work shows that the diffusive conductivity term in Eq. (22) is indeed required to capture a threshold instability condition in our flow. The model of Hoburg and Melcher,<sup>10</sup> who explored a configuration similar to ours (with a conductivity gradient perpendicular to applied field) neglected this term as their flow length scales of interest were larger than those of our  $100 \times 1000 \mu\text{m}$  channel cross-section. Our convective electroosmotic flow boundary conditions (see next section) are also a new characteristic not found in the initially stationary-liquid EHD work. Another difference between this and the work of Hoburg and Melcher is that we consider a more realistic conductivity profile consistent with our experiments. (Note that Hoburg and Melcher also used a more realistic diffusive profiles in later studies of different flow configurations, see for example, Ref. 18.) Lastly, we consider both two- and three-dimensional flows, and solve the fully nonlinear equations in the two-dimensional case.

### C. Boundary conditions

In our analysis we shall assume periodicity in the streamwise ( $x$ ) direction, and prescribe the following (dimensionless) boundary conditions on the walls:

$$\nabla \phi \cdot \mathbf{n} = 0, \tag{23}$$

$$\nabla \sigma \cdot \mathbf{n} = 0, \tag{24}$$

$$\mathbf{v} \cdot \mathbf{t} = \frac{1}{R_v} \zeta \mathbf{E} \cdot \mathbf{t}, \tag{25}$$

$$\mathbf{v} \cdot \mathbf{n} = 0, \tag{26}$$

where  $\mathbf{t}$  and  $\mathbf{n}$  are the tangential and normal vectors of the wall, respectively. Equations (23) and (24) are respectively the condition that the boundary is nonconductive, and that there is no ion diffusion across the boundaries; Eq. (26) is the condition that the wall is impenetrable. Special attention should be paid to Eq. (25). This equation is simply the dimensionless form of the Helmholtz–Smoluchowski formula-

tion (11), but with  $\zeta$  being a function of local conductivity, and  $\mathbf{E}$  being the instantaneous local electric field. Our non-dimensionalization gives us another dimensionless group

$$R_v \equiv \frac{E_o H}{-\zeta_o} \sim 5.6 \times 10^{-3}, \tag{27}$$

which represents the electroviscous to electroosmotic velocity ratio.

To close the system Eq. (25) can be combined with the following approximate empirical correlation for the nondimensional zeta potential:

$$\zeta = \left( \frac{C}{C_R} \right)^n,$$

where  $C_R$  is a reference concentration at which  $\zeta^* = \zeta_o = -7 \times 10^{-2} \text{ V}$ . We take its dimensional value as  $C_R^* = 1.0 \text{ mol/m}^3$ , which correspond to a dimensionless value of  $C_R \approx 30$  in our current scheme of nondimensionalization. For the power index  $n$ , classical EDL theory would suggest a value of  $n = -1/2$ , which assumes a constant surface charge density.<sup>7</sup> However, more recent models of EDL physics (Scales *et al.*<sup>30</sup>) suggest a somewhat weaker dependence of  $\zeta$  on ion density. In this paper, we assume an approximate value of  $n = -1/3$  as suggested by the experimental work of Yao *et al.*<sup>31</sup> who measured zeta potentials of borosilicate surfaces. Our diffusive ohmic model formulation, therefore, couples with the physics of the EDL only through a slip velocity which is dependent on local ion density.

Lastly, note that in nondimensional terms  $\sigma \approx 2C$  from the electroneutrality assumption.

## IV. TWO-DIMENSIONAL MODEL

In this section we assume that the flow exists only in the  $x$ - $y$  plane, with no dynamics in the  $z$  direction. This analysis will capture the basic physics of the instability mechanisms due to the conductivity gradient. As we discuss in the next section, the primary defect of this model is the neglect of the influence from the side walls in the  $x$ - $y$  plane. The experimental channel is “shallow” (in  $z$ ) compared to the height (in  $y$ ). (Here we refer to a channel as shallow if its aspect ratio  $[z]/[y] \ll 1$ , and “deep” if  $[z]/[y] \gg 1$  such that the two-dimensional simplification can be assumed.) Despite its limitations, the two-dimensional model provides a framework to understand the full three-dimensional physics and the experimental results.

We will start the section by conducting a linear stability analysis of the governing equations to analyze the behavior of the system. We follow by a two-dimensional nonlinear simulation to demonstrate the basic features of the simulated flow and draw comparisons to the experiments.

### A. Linear analysis

We use a linear stability analysis to predict the regimes where we would expect rapid mixing to occur. We start by defining a base state that satisfies the governing equations. The base state is assumed to be a function of  $y$  and  $t$  only. This simple assumption, coupled with two-dimensionality

and continuity, demand that velocity field in  $y$  is zero. The base state of conductivity  $\sigma_0(y, t)$  thereby obeys the simple diffusion equation

$$\frac{\partial \sigma_0}{\partial t} = \frac{1}{Ra_e} \nabla^2 \sigma_0,$$

subjected to the Neumann boundary condition  $[\partial \sigma_0 / \partial y]_{y=\pm 1} = 0$ . To determine  $\sigma_0(y, t=0)$  we solve a preliminary problem where the upper and lower halves of the channel are assumed to be of uniform, but differing conductivities separated by an infinitely sharp gradient. The interface is allowed to diffuse for a time equal to the advection time from the channel inlet to the viewing area of the experiment. The resulting conductivity profile is then used as an initial condition to the instability analysis.

The difference in the conductivity in the two channel halves induces different electroosmotic velocities at the upper and lower boundaries of the channel. The resulting base state flow field under these assumptions is a sheared Couette flow

$$u_0 = \frac{U_1 + U_{-1}}{2} + y \frac{U_1 - U_{-1}}{2}, \quad (28)$$

where the velocities at the boundaries ( $U_1$  and  $U_{-1}$ ) are provided by Eq. (25). The base values for the generated electric potential and charge density are zero.

The base solution satisfies the governing equations, and we check the stability of this base state with respect to small perturbations. We assume periodicity in  $x$  and expand the base solution in normal modes as  $f = f_0(y, t) + \epsilon \hat{f}(y, t) e^{ikx}$ , where  $\epsilon$  is a small parameter.<sup>32</sup> The linearized equations for the disturbances read

$$0 = -ik\hat{\sigma} + \sigma_0 \nabla^2 \hat{\phi} + \frac{d\sigma_0}{dy} \frac{\partial \hat{\phi}}{\partial y}, \quad (29)$$

$$\frac{\partial \hat{\sigma}}{\partial t} = -iku_0 \hat{\sigma} - \hat{v} \frac{d\sigma_0}{dy} + \frac{1}{Ra_e} \nabla^2 \hat{\sigma}, \quad (30)$$

$$ik\hat{u} + \frac{\partial \hat{v}}{\partial y} = 0, \quad (31)$$

$$\frac{\partial \hat{u}}{\partial t} = -iku_0 \hat{u} - \hat{v} \frac{du_0}{dy} + \frac{1}{Re} (-ik\hat{p} + \nabla^2 \hat{u} - \nabla^2 \hat{\phi}), \quad (32)$$

$$\frac{\partial \hat{v}}{\partial t} = -iku_0 \hat{v} + \frac{1}{Re} \left( -\frac{\partial \hat{p}}{\partial y} + \nabla^2 \hat{v} \right), \quad (33)$$

where

$$\nabla^2 \equiv \left( \frac{\partial^2}{\partial y^2} - k^2 \right).$$

The boundary conditions become

$$\frac{\partial \hat{\phi}}{\partial y} = 0, \quad (34)$$

$$\frac{\partial \hat{\sigma}}{\partial y} = 0, \quad (35)$$

$$\hat{u} = -u_o \left( \frac{1}{3} \frac{\hat{\sigma}}{\sigma_o} + ik\hat{\phi} \right), \quad (36)$$

$$\hat{v} = 0. \quad (37)$$

The time dependence of the base state introduces a non-homogeneous function in time that prevents us from assuming the standard separable temporal growth  $e^{st}$ . We can make a quasi-steady assumption for the base state and conduct a traditional linear stability analysis replacing the time derivatives in the above equations as  $\partial/\partial t = s$ . This quasi-steady assumption is accurate when the growth rate of the perturbation is rapid with respect to the time scale of diffusion of the base state conductivity, which is the case of interest when predicting rapid mixing regimes. When the growth rate of the disturbance is very slow (i.e., just above neutral stability), the streams will significantly mix via molecular diffusion before the disturbance waves grow large enough to begin to nonlinearly fold the two fluid streams. To verify the accuracy of our assumption we have solved the linearized equations above with and without this quasi-steady assumption; for the latter we solve the full time-dependent, initial value problem. We find that the linear flow evolution is identical for either solution method when the growth rate of the perturbation is “large” (we shall define a large growth rate via a mixing criterion below).

The linearized equations are solved using standard pseudo-spectral techniques with Chebyshev polynomials as the basis functions. Under the quasi-steady assumption we replace the time derivatives in Eqs. (29)–(37) with the eigenvalue  $s$ , and solve for the eigenvalues and eigenfunctions, using the methods outlined in such references by Trefethen<sup>33</sup> and Weidman.<sup>34</sup> The time dependent simulations of the linearized equations employed spectral methods as well, using the techniques outlined by Peyret.<sup>35</sup> For both methods we find that 64 points provides adequate resolution at reasonable computational cost.

## B. Linear results

We have obtained, for each wave number  $k$  and applied field  $E_o$ , a set of eigenvalues (the growth rate  $s$ ), together with their respective eigenfunctions. In Fig. 3 we show a contour plot of the growth rates of most unstable eigenfunction in the wave number-electric Rayleigh number (electric field) parameter space. The neutral stability curve is obtained by setting  $s_r \equiv \text{real}(s) = 0$ . A threshold electric field can be determined from the minimal value of  $E_o$  on the neutral stability curve. Similar to the results of Baygents and Baldessari,<sup>11</sup> we found that the inclusion of the diffusive term  $(1/Ra_e)\nabla^2 \sigma$  in Eq. (22) is crucial for the existence of the neutral stability curve.

Nevertheless, the neutral stability curve is less interesting in our case for practical purposes. Recall that when the growth rate is close to zero, our quasi-steady assumption is not accurate, and the flow will significantly mix (and be smoothed) by molecular and momentum diffusion before there is sharp folding of the material. Here we define a fast growth that will serve as the demarcation between a mixed and unmixed flow in our analysis. This *ad hoc* kinematic

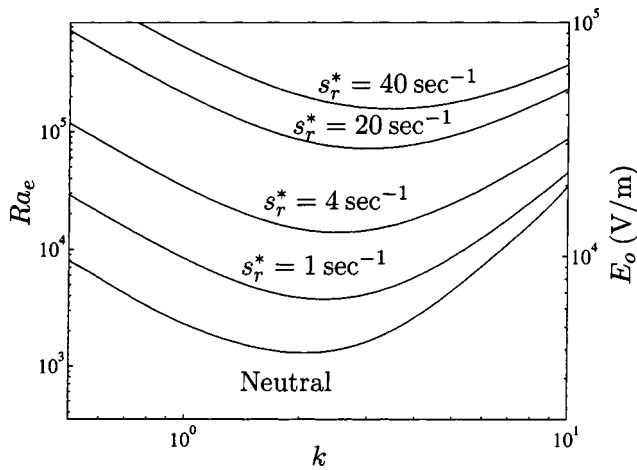


FIG. 3. Contour plot of growth rates ( $s_r^*$ ) versus wave number and electric Rayleigh number. Dimensional applied electric field is provided on the right axis. For the case plotted here, the initial interface of the two fluids approximately extends between  $-0.75 < y < 0.75$  and the ratio of the conductivity between the two streams is 10.

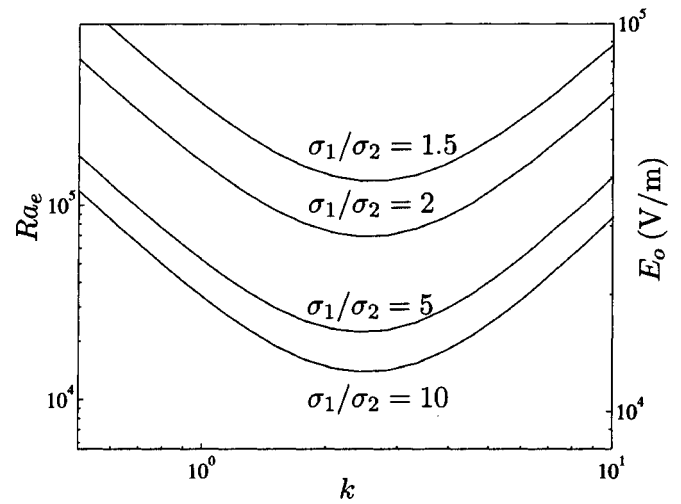


FIG. 4. Comparison of the contour corresponding to the  $s_r^* = 4 \text{ s}^{-1}$  growth rate for the same parameters as Fig. 3, but shown for various conductivity ratios. We see that the critical electric field required for mixing is lower as the conductivity ratio increases.

criterion is preferred over the neutral stability curve to facilitate a straightforward comparison with experiments where *observable* instability dynamics lead to rapid mixing. We denote a *dimensional* growth rate by

$$s_r^* \equiv s_r U_{ev} / H,$$

and set our rapid mixing criterion to be

$$s_r^* \sim 4 \text{ s}^{-1}. \tag{38}$$

A growth rate of this magnitude corresponds to the amplification of a perturbation by a factor of  $10^5$  in approximately three seconds. With this growth rate a disturbance of nanometer size will grow to 10% of the channel height in a few seconds. This growth rate should be observable in our experiments and will serve as a criterion between rapid and slow mixing regimes in our analysis. The necessity of this mixing criterion will be demonstrated later in Sec. IV C by nonlinear numerical simulations, where we will also discuss the scaling behavior of (i.e., the critical physical forces associated with) the instability dynamics.

Using the mixing criterion (38) we find that the two dimensional analysis under-predicts the mixing threshold when compared to the experimental data. The experiments show a strong transition to mixing occurring between applied fields of  $E = 2.5 \times 10^4 \text{ V/m}$  and  $E = 5 \times 10^4 \text{ V/m}$ , whereas the analysis predicts the mixing threshold to occur at approximately  $E = 1.25 \times 10^4 \text{ V/m}$ .

Using our model we also investigate the sensitivity of the mixing results to changes in conductivity ratio of the two streams. We keep the concentration of the lower stream fixed and vary the concentration of the upper stream. In Fig. 4 we show the predicted mixing boundary in wave number and electric field parameter space for various conductivity ratios. We see that the critical field is lowered for larger values of conductivity ratio across the stream. Note that this theory also predicts that the most dangerous wave number remains essentially unchanged ( $k \approx 2.5$ ) as the conductivity ratio changes. This trend is consistent with preliminary experi-

ments we have performed at conductivity ratios of 2, 5, and 10 which will be discussed in a future paper.

In Fig. 5 we show the unstable eigenfunctions of the linearized equations at an electric field of  $2.5 \times 10^4 \text{ V/m}$ . The stream function assumes the standard relation to the fluid velocity components as

$$\left( \frac{\partial \Psi}{\partial y}, -\frac{\partial \Psi}{\partial x} \right) = (u, v),$$

and is obtained through

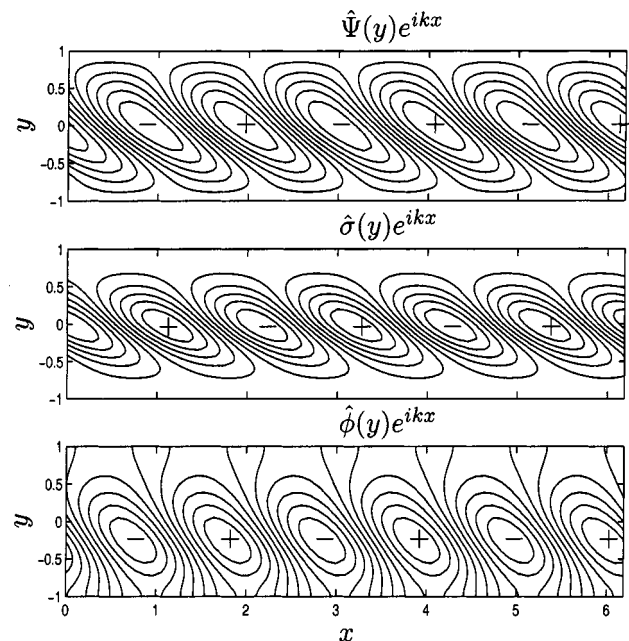


FIG. 5. Eigenfunctions of the most unstable mode for the  $2.5 \times 10^4 \text{ V/m}$  situation. The contour plot of the stream function, conductivity, and electric potential perturbations are shown. There is a set of nearly symmetric eigenfunctions that have streamlines that lean toward the left. The “+” and “-” signs denote the local maxima and minima of the plotted functions.

$$\Psi = \frac{i}{k} \hat{v}.$$

We show the disturbance functions for streamlines, conductivity, and electric potential.

For higher applied fields such that rapid mixing occurs, the most unstable modes almost always come in pairs, the (real) growth rates being nearly equal, and the eigenfunctions being nearly symmetric to each other. Compared with the exact symmetry (i.e., complex-conjugate eigenvalues, and eigenfunctions being mirror images) observed by Hoburg and Melcher,<sup>10</sup> the slight asymmetry of our eigenvalues and eigenfunctions is due to our base electroosmotic flow. Take for example the case of  $E_o = 25000$  V/m, at the most unstable wave number  $k=3$ , the most unstable eigenvalue is  $s = 0.0371 - 0.09i$ , which translates to a dimensional growth rate of  $s_r^* \sim 16$  s<sup>-1</sup>, and a right-traveling wave speed of  $s_i^*/k^* \sim 6.6$  mm/s. The paired eigenmode assumes a value of  $s = 0.0336 + 0.013i$ , which translates to a dimensional growth rate of  $s_r^* \sim 15$  s<sup>-1</sup>, and a left-traveling wave speed of  $s_i^*/k^* \sim -1.2$  mm/s. On the other hand, if we set the base shear flow as defined by (28) to be  $u_o = 0$ , we recover the symmetry and obtain  $s = 0.0366 \pm 0.0522i$ , or  $s_r^* \sim 16$  s<sup>-1</sup>, and waves traveling to the right and left at equal speeds of  $\sim 3.8$  mm/s. Therefore including the electroosmotic base state (28) causes a shift of wave speed in the direction of electroosmotic flow. The magnitude of the shift is  $\sim 2.7$  mm/s, which agrees almost exactly with the average value of  $u_o$  from Eq. (28), i.e.,  $(U_+ + U_-)/2 \sim 2.8$  mm/s.

Aside from the phase speed change in the instability waves, the electroosmotic velocity does not have a strong influence on the stability physics for our current parameter range of interest. Nonetheless in a simultaneous work by three of us (C.H.C., H.L., J.G.S. together with S. K. Lele), the electroosmotic velocity is found indeed important for a different parameter range, and a critical value of  $R_v$ , which is defined as the ratio of electroviscous to electroosmotic velocity, serves to demarcate between absolute and convective instability [see C.-H. Chen, H. Lin, S. K. Lele, and J. G. Santiago, "Convective and absolute electrokinetic instability with conductivity gradients," *J. Fluid Mech.* (submitted)]. We refer the readers to that study for details. For the current paper, we simply point out that because  $R_v \ll 1$  [Eq. (27)], electroosmotic flow has only minor influence, and our instability is dominantly absolute in nature, which is consistent with the temporal growth of the instability waves.

### C. Two-dimensional (2D) numerical simulation

We solve the governing Eqs. (14)–(16) and (21)–(26) numerically to capture the nonlinear evolution of the instability observed in the experiments. The initial conditions are the base states that have been discussed in the linear analysis, and a white noise perturbation is supplied with an amplitude of  $10^{-5}$  with respect to the base state.

The equations are solved using a pseudo-spectral collocation method. We use Chebyshev polynomials to expand the equations in the cross stream direction, and Fourier series in the streamwise direction. The details on the implementation

of similar problems are found in the literature.<sup>33,35</sup> The nonlinear terms are explicitly integrated forward in time using a second-order Adams–Bashforth scheme, while diffusive terms are integrated using a Crank–Nicholson scheme to achieve numerical stability. The momentum equation is solved with the velocity–pressure formulation outlined by Peyret.<sup>35</sup> Resolution of 64 points in both directions provides adequate results, and finer grids were used to test for convergence. The methods we used are standard and well-documented; we will not provide the details herein. To aid in direct comparison with the experimental visualizations, we solve an advection–diffusion equation for a passive tracer with a  $3 \times 10^{-11}$  m<sup>2</sup>/s diffusivity to simulate the motion of the dye molecules observed in the experiments. Because the dye has a much lower diffusivity (compared with  $2 \times 10^{-9}$  m<sup>2</sup>/s for the electrolytes), it avoids the diffusive effects in numerical visualization, exhibits a sharper interface, and better characterizes material line distortions observed in experiments. (In fact we shall show in Sec. IV D that for the more violently unstable regime, i.e., the high electric Rayleigh number dynamics, diffusion of the conductivity field is largely negligible so that the observed dye follows closely the evolution of the conductivity field.)

First we demonstrate the necessity of the mixing criterion (38) as we have proposed in Sec. IV B. Shown in Fig. 6 is the nonlinear evolution of the instability at applied fields of 6250, 8500, and 12500 V/m. The linear theory predicts growth rates of  $s_r^* = 1, 2,$  and  $4$  s<sup>-1</sup>, respectively. Each column of snapshots corresponds to different growth rates as given by higher driving electric fields. In the first column of Fig. 6, the distribution of the dye is governed by molecular diffusion, even though the linear stability analysis demonstrates that the flow is unstable. The simulation evolves for 18 seconds before we see visual evidence of waves. As we increase the electric field to observe different growth rates we see that the instability can begin to mix the flow more rapidly than molecular and momentum diffusion can smooth it. The main point to be taken concerning Fig. 6 is that there is a regime where the quasi-steady analysis predicts the flow to be unstable, but the growth rate is not sufficient to be of practical interest as a rapid effect.

In Fig. 7 we show the nonlinear evolution of the simulated dye field at stronger electric fields. The two right columns have applied fields stronger than those shown in Fig. 6 and are well within the rapid mixing regime. For comparison we also show in the left column the case of  $E_o = 10000$  V/m which is just below the rapid-mixing threshold. The model reproduces many of the essential features observed in the experiments, including the shape and initial break-up dynamics of the interface, the transverse growth of a wave pattern in the interface, and a roll-up of scalar structures observed at later times. Note the similarity in the most unstable (and most apparent) wave number at later times between the simulation and experiments.

Despite similarities between wave number and the dynamics of the interface breakup, the threshold imposed fields from both the linear and nonlinear predictions are lower than those shown for the experiment in Fig. 2. [In fact, the *ad hoc* criterion (38) was suggested to us by the nonlinear simula-

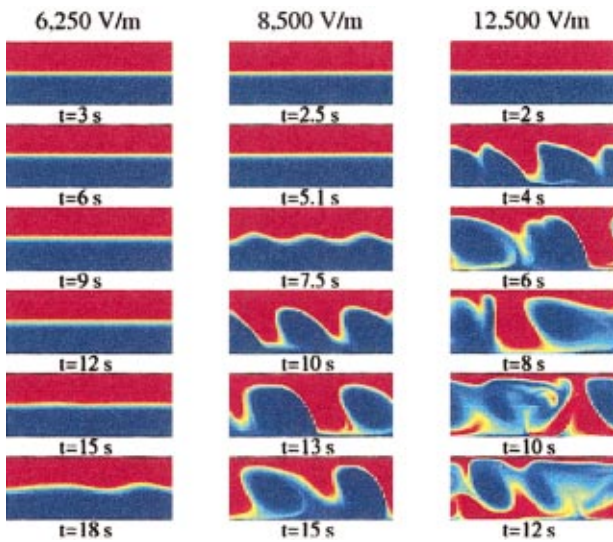


FIG. 6. (Color) Snapshots of the dye field at various instances in time for different driving electric fields. The electric fields (applied at  $t=0$ ) and bulk flow are directed from left to right. Each column indicates a different applied field and the rows within each column present selected snapshots in time. The image correspond to a physical domain of  $3.6\text{ mm} \times 1\text{ mm}$ . (Note that the images have been slightly stretched in the  $y$  direction to give best visualization.) The left-hand column corresponds to an applied field of  $E=6250\text{ V/m}$ , the middle column to  $E=8500\text{ V/m}$ , and the right-hand column to  $E=12500\text{ V/m}$ , and the linearly predicted growth rates are  $s_r^*=1\text{ s}^{-1}$ ,  $s_r^*=2\text{ s}^{-1}$ , and  $s_r^*=4\text{ s}^{-1}$ , respectively. The time for noticeable waves to develop is decreased as the field is increased. For the purposes of this paper, we decide that the mixing provided by  $s_r^*=4\text{ s}^{-1}$  indicates a well-mixed flow in the times of practical interest.

tions shown in Fig. 6.] For example, compare the evolution of the dye at  $25000\text{ V/m}$  from the experiments (Fig. 2, column 1) and the simulation (Fig. 7, column 3). We see that the simulation at  $25000\text{ V/m}$  predicts a well-stirred flow field in less than three seconds while experiments show that the flow is stable on the time scale of the experiments. The simulation of  $25000\text{ V/m}$  is qualitatively similar to the experimental flow at  $75000\text{ V/m}$  (Fig. 2, column 3). Despite the discrepancy in the magnitude of the applied field, our simulation captures a threshold field and scalar features qualitatively similar to the experiment. In Sec. V we will try to address possible causes for the under-prediction of the threshold electric field by including three-dimensional effects.

### D. Discussion

In both our linear and nonlinear calculations we have given our results in *dimensional* units, i.e., we used the dimensional field strength to determine instability threshold, and a dimensional growth rate to quantify instability growth rate. This approach has been adopted primarily to facilitate direct comparisons with experiments. In this section we turn to discuss the scaling characteristics of the instability, particularly in light of the electroviscous scaling proposed by Hoburg and Melcher.<sup>10</sup>

In Hoburg and Melcher<sup>10</sup> the authors defined an electroviscous time

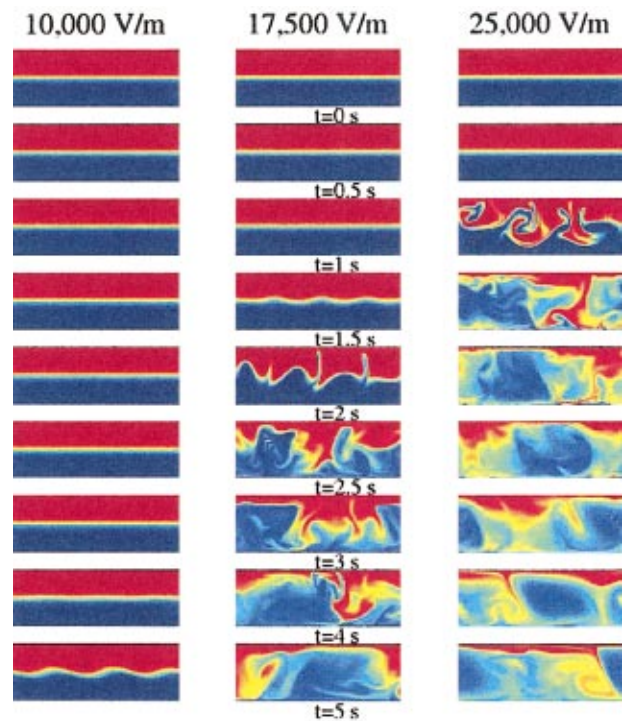


FIG. 7. (Color) Sample images from the nonlinear numerical simulations for three different applied fields (columns) and various times (rows). The electric field and bulk flow are directed from left to right. High field is applied at  $t=0\text{ s}$ . Each image corresponds to a visualization of a passive scalar in a physical domain of  $1\text{ mm}$  wide ( $y$ ) by  $3.6\text{ mm}$  long ( $x$ ); the  $z$  (depth) dimension is not modeled in these simulations. (Note that the images have been slightly stretched in the  $y$  direction to give best visualization.) An initial white-noise perturbation with an amplitude of  $10^{-5}$  with respect to the base state is provided. The images display a passive tracer that has the diffusivity of the dye used in the experiments. The images in each row are taken at the same time as shown in the figure.

$$\tau_{ev} \equiv \frac{H}{U_{ev}} = \frac{\mu}{\epsilon E_o^2}, \tag{39}$$

and demonstrated that instability growth rates scale as  $\tau_{ev}$ . Here we examine this instability scaling behavior using our nonlinear simulations. In Fig. 8(a) we plot dimensional velocity as a function of dimensional time for various applied fields; the velocity  $v_{\text{max}}$  is defined as the maximum transverse velocity in the nonlinear simulations at each instant. For each applied field (with the exception of the lowest),  $v_{\text{max}}$  grows exponentially to a peak value consistent with the most vigorous stage of the instability, and then relaxes to a slowly decaying value as a well-mixed state is achieved. The curves show the general trend that for higher field, the instability grows faster, and a higher peak value for  $v_{\text{max}}$  is obtained. In Fig. 8(b), we scale  $v_{\text{max}}$  and  $t$  with the electroviscous scales  $U_{ev}$  and  $\tau_{ev}$ , respectively. Under this scaling, we find the dynamics of  $v_{\text{max}}$  nicely collapse to a single curve for a wide range within the strongly unstable regime ( $E_o = 8500, 17500, \text{ and } 25000\text{ V/m}$ ). Note that these three evolution curves nearly exactly overlap, with identical dimensionless growth rates and peak values of  $v_{\text{max}}/U_{ev}$ . In contrast, we also observe minor deviations from the

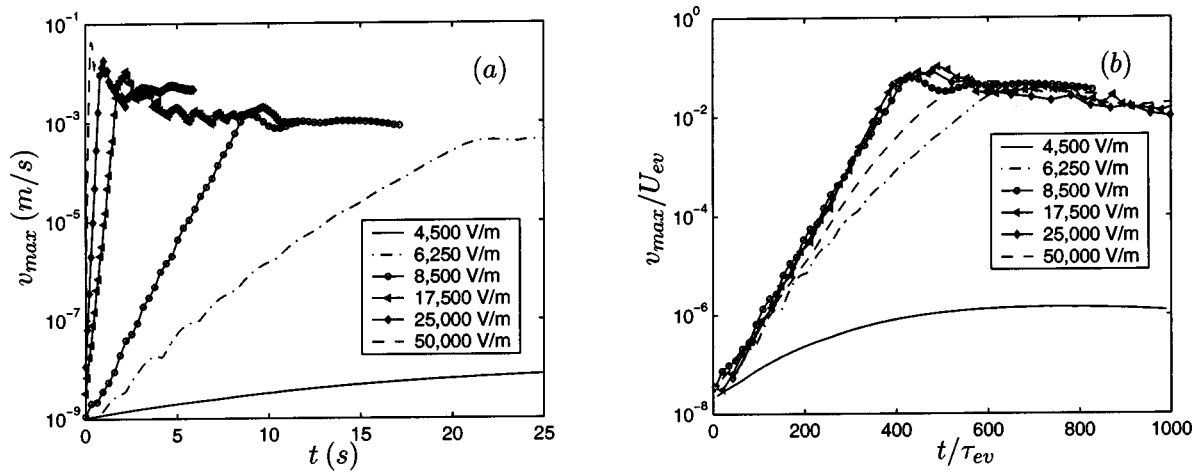


FIG. 8. Demonstration of the electroviscous scaling. For both graphs, simulations at electric fields of  $E_o = 4500$  (solid), 6250 (dash-dot), 8500 (circles), 17500 (triangles), 25000 (diamonds) and 50000 (dash) V/m are shown. In (a) we plot a dimensional  $v_{\max}$  as a function of the dimensional time  $t$ , where  $v_{\max}$  is defined as the maximum transverse velocity in the field at each instant from the nonlinear simulations. In (b) we scale  $v_{\max}$  and  $t$  with  $U_{ev}$  and  $\tau_{ev}$ , respectively. The modeling shows that, for a wide range of electric fields (from 8500 to 25000 V/m) of interest here, the various curves collapse almost identically to a single curve which grows exponentially, overshoots a critical value, and then damps down slowly as mixing progresses. The collapse of the curves validates the electroviscous processes as the dominant dynamics over most of the range of interest. The 6250 V/m (dash-dot) and 50000 (dash) V/m cases show significant deviation from electroviscous scaling due to increased molecular diffusion and inertial effects, respectively. In the 4500 V/m (solid) case (close to the instability threshold), molecular diffusion dominates the development of the field and the electroviscous scaling is no longer valid.

electroviscous behavior at  $E_o = 6250$  and 50000 V/m, and a major deviation at  $E_o = 4500$  V/m when the field strength approaches the instability threshold.

The collapse of the dynamics of  $v_{\max}$  for the mid-range of the significantly unstable regime is well explained by the electroviscous time and velocity scaling arguments of Hoburg and Melcher.<sup>10</sup> The limitation of this scaling at high and low electric field values can be explained by comparing the electroviscous time to the time scales of molecular and momentum diffusion. In Hoburg and Melcher<sup>10</sup> the authors define a momentum diffusion time scale as

$$\tau_v \equiv \frac{\rho H^2}{\mu} \sim 0.25 \text{ s}, \quad (40)$$

which signifies the relative importance of the inertial force in the momentum equation. As suggested by the work of Baygents and Baldessari,<sup>11</sup> we also have yet another important time scale, the diffusion time

$$\tau_d \equiv \frac{H^2}{D} \sim 125 \text{ s}. \quad (41)$$

Ratios of these times scales yield dimensionless numbers we defined earlier:

$$Re = \frac{\tau_v}{\tau_{ev}} \propto E_o^2, \quad Ra_e = \frac{\tau_d}{\tau_{ev}} \propto E_o^2, \quad (42)$$

and both these numbers increase quadratically as applied field increases. For higher values of the field strength (such as the  $E_o = 50000$  V/m case in Fig. 8), the electric-field-driven flow is characterized by a Reynolds number of order unity or greater, and so inertial forces affect the dynamics of the instability and we expect deviations from the electroviscous behavior. However, as pointed out in Hoburg and Melcher,<sup>10</sup> the dependence of the instability dynamics on  $Re$  is weak in this regime, and so the deviation is apparent but

not dramatic. For lower values of field strength (such as the 6250 V/m case in Fig. 8), on the other hand, deviations from the electroviscous behavior is due to the increased relative importance of the simple molecular diffusion associated with small electric Rayleigh numbers and a (relatively) small diffusive time scale  $\tau_d$ . As one further decreases the field strength to approach the instability threshold (e.g., the  $E_o = 4500$  V/m case of Fig. 8), molecular diffusion plays the dominant role in the development of the flow field and the electroviscous scaling is no longer valid. The growth of disturbances is mostly quenched by diffusion and only marginal instability is observed.

Note that even though the electroviscous velocity and times scales adequately collapse the instability dynamics across applied fields, the absolute values of these scales tend to be significantly larger than the values observed in the nonlinear simulations. For example, the characteristic values of the scaled, nondimensional velocity and time scales in Fig. 8(b) are of order 0.1 and  $10^3$ , respectively. (A similar conclusion is found in scaling the streamwise disturbance velocity  $u_{\max}$ .) However, the derived electroviscous velocity and time scales used here are based on simplified scaling arguments and are not directly observed quantities in an experiment (i.e., these are estimates of the internal physical scales and not quantities directly imposed by the experimentalist). Therefore, although these electroviscous scales correctly scale the dynamics, caution should be used in applying these derived scales to identify dynamic regimes of the generalized formulation. For example, the value of the electric Rayleigh number based on the derived electroviscous velocity scale [Eq. (17)] for the  $E_o = 6500$  V/m case in Fig. 8 is  $Ra_e \approx 3400$ , suggesting that diffusive effect can be safely ignored. However, as our numerical simulation [Fig. 8(a), dot-dash] finds, an effective time scale for the instability growth in this case is  $\tau_{\text{eff}} \approx 20$  s, which gives an effective Rayleigh

number of  $Ra_{\text{eff}} \equiv \tau_d / \tau_{\text{eff}} \approx 6$ , and which suggests diffusion processes are important [Fig. 8(b), dot-dash]. (This trend of over-prediction becomes more prominent as one approaches the instability threshold, e.g., for the  $E_o = 4500$  V/m case, where the electroviscous scaling is no longer valid.)

### V. THREE-DIMENSIONAL MODEL

In the previous sections we have provided a two-dimensional framework that appears to capture the primary physics of our flow. The primary limitation in our model is the two-dimensional assumption. The channel in the experiment is shallow, with an aspect ratio of  $[z]/[y] = 0.1$ . In the two-dimensional model, we assumed that EDL's formed on the upper and lower ( $y = \pm 1$ ) boundaries of the channel and drove a linear Couette flow. In the actual three-dimensional case, an EDL also forms along the side walls ( $z = \pm \delta$ , where  $\delta \equiv d/H$ , and  $d$  is the half-depth of the channel), and strongly drives the flow due to the small depth of the channel. The three-dimensional flow base state is, therefore, not a simple Couette profile. Also, the three-dimensional nature of a thin channel couples the instability dynamics to the side walls via viscous forces. Below, we present a preliminary assessment of these three-dimensional effects using a linearized analysis. A fully nonlinear three-dimensional investigation will be presented in a future paper.

#### A. Base state

The base state is assumed to be invariant in the  $x$ -direction and the initial conductivity field is assumed a function of  $y$  only. By Eq. (21) we find that the conductivity field induces no electric field, and therefore, does not directly couple to the momentum equation. The base state conductivity, therefore, evolves as

$$\frac{\partial \sigma_0}{\partial t} = \frac{1}{Ra_e} \frac{\partial^2 \sigma_0}{\partial y^2}, \quad (43)$$

subjected to Neumann boundary conditions at  $y = \pm 1$  and  $z = \pm \delta$ .

The base state velocity field is determined by the relationship between the zeta potential and the conductivity of the fluid at the wall. The flow is driven by the EDL at the walls  $y = \pm 1$  and  $z = \pm \delta$ . The velocity in the  $y$  and  $z$  directions are both zero as provided by continuity and the assumption of invariance in the  $x$ -direction. The base state velocity field is determined by the momentum equation

$$\frac{\partial u_0}{\partial t} = \frac{1}{Re} \left( \frac{\partial^2}{\partial y^2} + \frac{\partial^2}{\partial z^2} \right) u_0, \quad (44)$$

subject to the boundary conditions

$$u_0 = \frac{1}{R_v} \zeta(\sigma_0), \quad (45)$$

at the walls  $y = \pm 1$  and  $z = \pm \delta$ . In the application of interest the electric Rayleigh number is large in comparison to the Reynolds number, such that the time-dependent term in the momentum equation can be neglected. [Recall that the velocity boundary condition is coupled to the conservation of con-

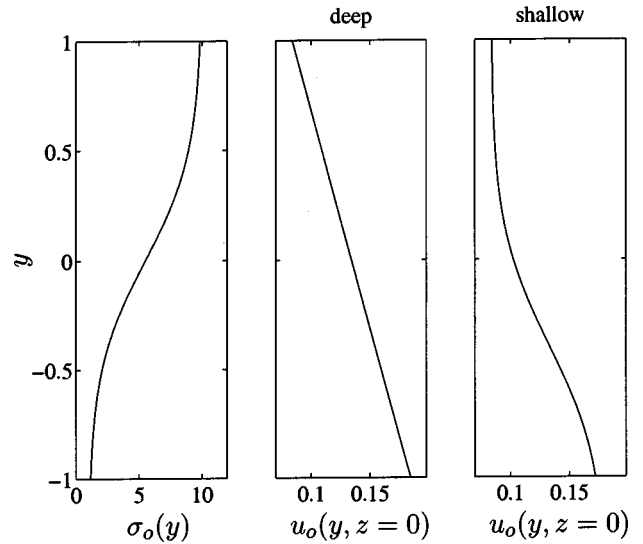


FIG. 9. Base state conductivity (left-hand plot) and velocity profiles for a channel that is deep (middle plot) and shallow (right-hand plot) in the spanwise,  $z$  direction into the page as shown in Fig. 7. In both cases, axial velocity profile along the transverse  $y$  direction is shown for the mid-plane along  $z = 0$ . When the channel is deep and the effects of side walls are negligible, the flow is dominated by the EDL slip velocity that forms at the top and bottom walls at  $y = \pm 1$ , resulting in a linear shear. When the channel is shallow, the flow is dominated by the EDL velocity on the side walls (in the  $x$ - $y$  plane), and the flow field follows closely the shape of the conductivity profile.

ductivity relation via (25)]. Note that in the three-dimensional case with an added  $z$ -dimension, the flow is better characterized by a new effective Reynolds number  $Re_d \equiv Ud/v$ . However, for simplicity, we will continue to use the Reynolds number defined earlier and the statements presented here are still true since  $Re_d < Re$ . The conductivity slowly diffuses while the velocity field instantaneously corrects itself to the new boundary condition. The base state velocity field is therefore well approximated by

$$0 = \left( \frac{\partial^2}{\partial y^2} + \frac{\partial^2}{\partial z^2} \right) u_0, \quad (46)$$

subjected to boundary condition (45).

In Fig. 9 we compare the velocity profile as a function of  $y$  along the plane  $z = 0$  for the deep (two-dimensional) and shallow (three-dimensional) EK channels. For deep channels the flow behaves as a Couette flow as previously assumed. For shallow channels, the flow closely follows the EDL velocity along the side walls.

#### B. Linearized model

Again we investigate the stability character of the base state by linear analysis. We assume that all variables can be expanded as the base flow plus a small perturbation of a single Fourier mode  $f = f_0(y, z, t) + \epsilon \hat{f}(y, z, t) e^{ikx}$ . The governing equations for the perturbations read

$$Re \left( \frac{\partial \hat{u}}{\partial t} + ik u_0 \hat{u} + \hat{v} \frac{\partial u_0}{\partial y} + \hat{w} \frac{\partial u_0}{\partial z} \right) = -ik \hat{p} + \nabla^2 \hat{u} + \hat{\rho}_E, \quad (47)$$

$$Re \left( \frac{\partial \hat{v}}{\partial t} + iku_0 \hat{v} \right) = -\frac{\partial \hat{p}}{\partial y} + \nabla^2 \hat{v}, \quad (48)$$

$$Re \left( \frac{\partial \hat{w}}{\partial t} + iku_0 \hat{w} \right) = -\frac{\partial \hat{p}}{\partial z} + \nabla^2 \hat{w}, \quad (49)$$

$$\nabla^2 \hat{\phi} = -\hat{\rho}_E, \quad (50)$$

$$ik \hat{\sigma} = \sigma_0 \nabla^2 \hat{\phi} + \frac{\partial \sigma_0}{\partial y} \frac{\partial \hat{\phi}}{\partial y}, \quad (51)$$

$$\frac{\partial \hat{\sigma}}{\partial t} + iku_0 \hat{\sigma} + \hat{v} \frac{\partial \sigma_0}{\partial y} = \frac{1}{Ra_e} \nabla^2 \hat{\sigma}, \quad (52)$$

where

$$\nabla^2 \equiv \left( \frac{\partial^2}{\partial y^2} + \frac{\partial^2}{\partial z^2} - k^2 \right).$$

The boundary conditions become

$$\nabla \hat{\sigma} \cdot \mathbf{n} = 0, \quad (53)$$

$$\nabla \hat{\phi} \cdot \mathbf{n} = 0, \quad (54)$$

$$\hat{\mathbf{v}} \cdot \mathbf{t} = -u_o \left[ \frac{1}{3} \frac{\hat{\sigma}}{\sigma_o} \mathbf{e}_x + \nabla \hat{\phi} \right] \cdot \mathbf{t}, \quad (55)$$

$$\hat{\mathbf{v}} \cdot \mathbf{n} = 0, \quad (56)$$

where

$$\nabla \equiv \left( ik, \frac{\partial}{\partial y}, \frac{\partial}{\partial z} \right).$$

This formulation allows us to solve the time dependent problem evolution of a single Fourier mode in three dimensions, just as we have done in two-dimensions. In the three-dimensional case we elect to solve the time-dependent evolution rather than the complete eigenvalue problem. (The eigenvalue approach has not been adopted here; the computation for the three-dimensional case exhibits a poor scaling with respect to the number of grid points and is prohibitively expensive for our current numerical scheme.) We initialize the flow with a random perturbation in the  $y$  and  $z$  directions, and the growth rate for a single Fourier mode is extracted by fitting the disturbance amplitude to the function  $e^{st}$ . We apply the same rapid mixing criterion of  $s_r^* = 4 \text{ s}^{-1}$  as in the two-dimensional case.

The three-dimensional equations are again solved by pseudo-spectral methods as outlined by Peyret (2002).<sup>35</sup> We use Chebyshev polynomials as basis functions in the  $y$  and  $z$  directions. We again use the Adams–Bashforth method for integration of the convective terms and Crank–Nicholson for integration of the diffusive terms.

## C. Results

We now recreate Fig. 3 with the three-dimensional linear analysis and show the growth rate contours for  $\gamma = 10$  in Fig. 10. By adopting the same kinematic growth-rate criterion  $s_r^* = 4 \text{ s}^{-1}$ , the analysis predicts a critical electric field for

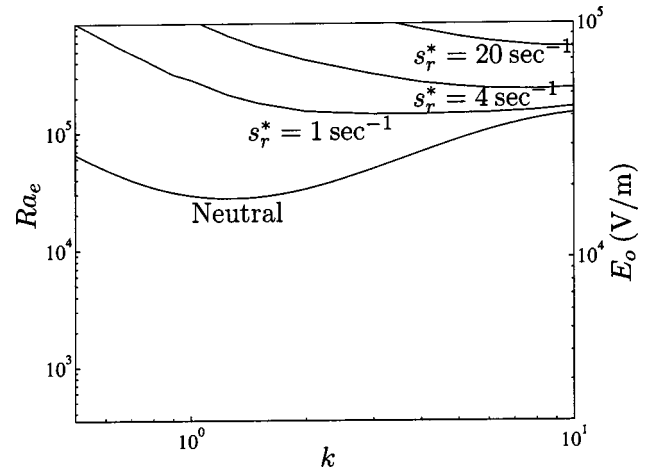


FIG. 10. Contour plot of growth rates  $s_r^*$  for different combinations of wave number and electric field using the three-dimensional analysis. In this case the interface of the two fluids approximately extends between  $-0.75 < y < 0.75$  and the ratio of the conductivity between the two streams is 10. This figure used the same parameters as Fig. 3 for the two-dimensional analysis. Compared to the two-dimensional model, the contours are shifted to higher electric fields indicating that the side walls stabilize the flow. [Note that we have shown the same ranges of  $Ra_e$  ( $E_o$ ) and  $k$  as in Fig. 3.]

mixing of approximately 50000 V/m for the conductivity ratio of 10, in closer agreement with the experimental data than the two-dimensional model.

In general when compared with the two-dimensional, infinite-depth analysis, we found that the critical electric field under the same conditions was much larger for the three-dimensional case for each of the conditions. The side boundaries in shallow channels (which can support a shear stress) act to stabilize the flow field. We also note that the linear three-dimensional model predicts a higher most-dangerous wave number at higher electric fields. However, which mode becomes the most rapidly growing in the fully nonlinear regime awaits further study with full nonlinear, three-dimensional simulations.

One interesting aspect of this problem is the difference in the physical mechanisms that exist in the two- and three-dimensional flows. In two-dimensions the instability originates purely from the within the conductivity gradient. In the three-dimensional case the flow is strongly coupled to the side walls. Due to the shallow channel depth and the low Reynolds number in the cross-stream direction, we expect that the electroosmotic flow in the channel to be quite uniform in the  $z$  direction, especially at the onset of the instability. This implies that the flow in the interior of the channel is deeply influenced by the velocity boundary condition on the side walls, which is in turn correlated to the generated electric field and the EDL. This side wall boundary condition provides a stabilizing force with respect to the instability dynamics due only to the conductivity gradient in the bulk liquid.

## VI. SUMMARY

We have presented experimental, numerical, and analytical results that explain the basic mechanisms behind an electrokinetic mixing phenomena observed in micro-fluidic

channels. We have presented analysis and computations based on different sets of assumptions for EK flows in a long, thin channel with a transverse conductivity gradient. Our analysis takes into account a shear imposed on the flow due to the dependence of zeta potential on local concentration and the effects associated with the diffusion of the conductivity scalar. In the first analysis we assumed that the flow was purely two-dimensional with neither variations in the  $z$  directions, nor influence from side walls. In the second analysis we accounted for the side walls and conducted three-dimensional linearized simulations. In both analyses we found a threshold electric field above which the flow becomes highly unstable and rapid mixing occurs. We also found that the coupling of the flow to the side walls in the three-dimensional model helps to stabilize the conductivity gradient. We have presented a mixing criterion useful for comparisons between model and experiments, and have explained key differences between the two- and three-dimensional analyses. We have confirmed the validity of the electroviscous scaling proposed by Hoburg and Melcher<sup>10</sup> with nonlinear numerical simulations, and discussed its range of validity. Our model is able to predict general trends in the data, and many of the basic aspects of the observed flow field. Our results demonstrate that the general framework as pioneered by Hoburg and Melcher,<sup>10</sup> and extended by Baygents and Baldessari,<sup>11</sup> is suitable for the study of EK instabilities provided boundary conditions, base states, and diffusion effects consistent with electroosmotic flow in microchannel systems are used. Future work will involve more detailed three-dimensional simulations to examine how the nonlinear regimes are impacted by the effect of the side walls.

The models presented in this work are useful in optimization studies, as parameter space can be spanned in simulations more quickly than in the laboratory. Work described by Oddy *et al.*<sup>27</sup> has demonstrated that oscillatory electric field can potentially drive even more vigorous mixing. The models presented in this work can be used to optimize the form of forcing functions, to design the shape of a micromixer, and to develop optimal control strategies for both micro-mixing and the suppression of instabilities.

## ACKNOWLEDGMENTS

This work was sponsored by DARPA (Contract No. F30602-00-2-0609) with Dr. Anantha Krishnan as contract monitor and by an NSF CAREER Award (J.G.S.) with Dr. Michael W. Plesniak as contract monitor. The authors thank James Hoburg for discussions and insights which significantly improved our work. B.D.S. would like to thank Burt Tilley for many helpful discussions and his suggestions on an early draft of this paper.

<sup>1</sup>A. Manz, N. Graber, and H. Widmer, "Miniaturized total chemical analysis systems: A novel concept for chemical sensing," *Sens. Actuators B* **1**, 244 (1990).

<sup>2</sup>G. H. W. Sanders and A. Manz, "Chip-based microsystems for genomic and proteomic analysis," *TrAC, Trends Anal. Chem.* **19**, 364 (2000).

<sup>3</sup>P. A. Auroux, D. Iossifidis, D. R. Reyes, and A. Manz, "Micro total analysis systems. 2. Analytical standard operations and applications," *Anal. Chem.* **74**, 2637 (2002).

<sup>4</sup>A. vandenBerg and T. S. J. Lammerink, "Micro total analysis systems:

Microfluidic aspects, integration concept, and applications," *Top. Curr. Chem.* **194**, 21 (1998).

<sup>5</sup>L. Bousse, C. Cohen, T. Nikifotov, A. Chow, A. Kopf-Sill, R. Dubrow, and J. Parce, "Electrokinetically controlled microfluidic analysis systems," *Annu. Rev. Biophys. Biomol. Struct.* **29**, 155 (2000).

<sup>6</sup>R. Probstein, *Physicochemical Hydrodynamics* (Wiley, New York, 1994).

<sup>7</sup>R. J. Hunter, *Zeta Potential in Colloid Science* (Academic, London, 1981).

<sup>8</sup>J. G. Santiago, "Electroosmotic flows in micro-channels with finite inertial and pressure forces," *Anal. Chem.* **73**, 2353 (2001).

<sup>9</sup>G. Batchelor, *An Introduction to Fluid Dynamics* (Cambridge University Press, London, 1967).

<sup>10</sup>J. F. Hoburg and J. R. Melcher, "Internal electrohydrodynamic instability and mixing of fluids with orthogonal field and conductivity gradients," *J. Fluid Mech.* **73**, 333 (1976).

<sup>11</sup>J. C. Baygents and F. Baldessari, "Electrohydrodynamic instability in a thin fluid layer with an electrical conductivity gradient," *Phys. Fluids* **10**, 301 (1998).

<sup>12</sup>D. A. Saville, "Electrohydrodynamics: The Taylor–Melcher leaky dielectric model," *Annu. Rev. Fluid Mech.* **29**, 27 (1997).

<sup>13</sup>W. B. Russel, D. A. Saville, and W. R. Schowalter, *Colloidal Dispersions* (Cambridge University Press, London, 1989).

<sup>14</sup>V. G. Levich, *Physicochemical Hydrodynamics* (Prentice Hall, Englewood Cliffs, NJ, 1962).

<sup>15</sup>J. R. Melcher, *Continuum Electromechanics* (MIT Press, Cambridge, 1981).

<sup>16</sup>J. R. Melcher and G. I. Taylor, "Electrohydrodynamics: A review of the role of interfacial shear stresses," *Annu. Rev. Fluid Mech.* **1**, 111 (1969).

<sup>17</sup>*Electrohydrodynamics*, edited by A. Castellanos (Springer-Verlag, New York, 1998).

<sup>18</sup>J. F. Hoburg and J. R. Melcher, "Electrohydrodynamic mixing and instability induced by colinear fields and conductivity gradients," *Phys. Fluids* **20**, 903 (1977).

<sup>19</sup>J. R. Melcher and W. J. Schwarz, "Interfacial relaxation overstability in a tangential electric field," *Phys. Fluids* **11**, 2604 (1968).

<sup>20</sup>Y. Ben, E. A. Demekhin, P. V. Takhistov, and H.-C. Chang, "Miscible fingering in electrokinetic flow," *J. Chin. Inst. Chem. Eng.* **33**, 15 (2002).

<sup>21</sup>D. S. Burgi and R. L. Chien, "Field amplified sample stacking (FASS): Optimization in sample stacking for high-performance capillary electrophoresis," *Anal. Chem.* **63**, 2042 (1991).

<sup>22</sup>A. E. Herr, J. I. Molho, K. A. Drouvalakis, J. C. Mikkelsen, P. J. Utz, J. G. Santiago, and T. W. Kenny, "On-chip coupling of isoelectric focusing and free solution electrophoresis for multidimensional separations," *Anal. Chem.* **75**, 1180 (2003).

<sup>23</sup>S. C. Jacobson and J. M. Ramsey, "Electrokinetic focusing in microfabricated channel structures," *Anal. Chem.* **69**, 3212 (1997).

<sup>24</sup>C. H. Chen and J. G. Santiago, "Electrokinetic instability in high concentration gradient microflows," *Proceedings of IMECE-2002*, New Orleans, LA, CD vol. 1, #33563 (2002).

<sup>25</sup>C. H. Chen, H. Lin, S. K. Lele, and J. G. Santiago, "Electrokinetic microflow instability with conductivity gradients," *Proceedings of  $\mu$ TAS2003*, Squaw Valley, CA (2003).

<sup>26</sup>J. M. Ramsey, S. C. Jacobson, and M. R. Knapp, "Microfabricated chemical measurement systems," *Nature Medicine* **1**, 1093 (1995).

<sup>27</sup>M. H. Oddy, J. G. Santiago, and J. C. Mikkelsen, "Electrokinetic instability and micromixing," *Anal. Chem.* **73**, 5822 (2001).

<sup>28</sup>R. Pottel, "Dielectric properties," in *Water: A Comprehensive Treatise*, edited by F. Franks (Plenum, New York, 1973), Vol. 3, p. 421.

<sup>29</sup>A. L. Horvath, *Handbook of Aqueous Electrolyte Solutions* (Wiley, New York, 1985).

<sup>30</sup>P. J. Scales, F. Grieser, and T. W. Healy, "Electrokinetics of the silica–solution interface: A flat plate streaming potential study," *Langmuir* **8**, 965 (1992).

<sup>31</sup>S. Yao, D. E. Hertzog, S. Zeng, J. C. Mikkelsen, and J. G. Santiago, "Porous glass electroosmotic pumps: Design and experiments," *J. Colloid Interface Sci.* **263**, 143 (2003).

<sup>32</sup>P. G. Drazin and W. H. Reid, *Hydrodynamic Stability* (Cambridge University Press, London, 1981).

<sup>33</sup>L. N. Trefethen, *Spectral Methods in MATLAB* (SIAM, Philadelphia, 2001).

<sup>34</sup>J. A. C. Weideman and S. C. Reddy, "A MATLAB Differentiation Matrix Suite," *ACM Trans. Math. Softw.* **26**, 465 (2000).

<sup>35</sup>R. Peyret, *Spectral Methods for Incompressible Viscous Flow* (Springer-Verlag, New York, 2002).

<sup>36</sup>The scale  $E_0$  we use here is close to the maximum electric field of interest in our problem, and  $\Delta C_0/C_0$  only decreases as imposed field decreases.